

Cell Reports Physical Science, Volume 3

Supplemental information

**Addressing solar photochemistry durability
with an amorphous nickel antimonate photoanode**

Lan Zhou, Elizabeth A. Peterson, Karun K. Rao, Yubing Lu, Xiang Li, Yungchieh Lai, Sage R. Bauers, Matthias H. Richter, Kevin Kan, Yu Wang, Paul F. Newhouse, Junko Yano, Jeffrey B. Neaton, Michal Bajdich, and John M. Gregoire

Supplemental Experimental Procedures

Tables S1-S3 provide experimental details for photoelectrochemistry experiments, including the calibration data required to calculate EQE as follows:

$$\text{External Quantum Efficiency (EQE)} = \frac{1240 \times \text{Photocurrent [A]}}{\text{Incident light wavelength [nm]} \times \text{Power [W]}}$$

EQE is also known as incident photon-to-current conversion efficiency (IPCE).

Table S1. Summary of electrolytes used in PEC measurements.

pH	Abbreviation	Electrolyte + (sacrificial hole acceptor)
1	MET1	0.1 M sulfuric acid + 0.25 M sodium sulfate + (0.1 M methanol)
7	SLF7	0.05 M potassium phosphate monobasic + 0.05 M potassium phosphate dibasic + 0.25 M sodium sulfate + (0.01 M sodium sulfite)
10	OER10	0.1 M boric acid + 0.085 M potassium hydroxide + 0.25 M sodium sulfate
10	SLF10	0.1 M boric acid + 0.085 M potassium hydroxide + 0.25 M sodium sulfate + (0.01 M sodium sulfite)

Table S2. Irradiance for SDC experiments in SLF7 and SLF10 in Figure 1 (measurement area = 2 mm²).

LED (eV) (Doric LEDC4)	Power (mW)	Irradiance (mW cm⁻²)
3.20 ± 0.05	3	150
2.72 ± 0.08	2.18	109
2.41 ± 0.08	0.92	46
2.06 ± 0.03	0.42	21

Table S3. Irradiance for SDC experiments in MET1 in Figure 1 (measurement area = 2 mm²).

LED (eV) (Doric LEDC4)	Power (mW)	Irradiance (mW cm⁻²)
3.20 ± 0.05	2.93	146.5
2.72 ± 0.08	2.48	124
2.41 ± 0.08	1.05	52.5
2.06 ± 0.03	1	50

Supplemental Notes

Supporting data include Pourbaix analysis (Figure S1), PEC (Figure S2), XPS (Figures S3-S4), TEM (Figures S5-S6), TEM with PEC on an additional sample (Figure S7), XAS (Figures S8-S10 and Table S4), optical spectroscopy (Figure S11), DFT (Figures S12-S14 and Table S5), and comparisons with literature (Table S6).

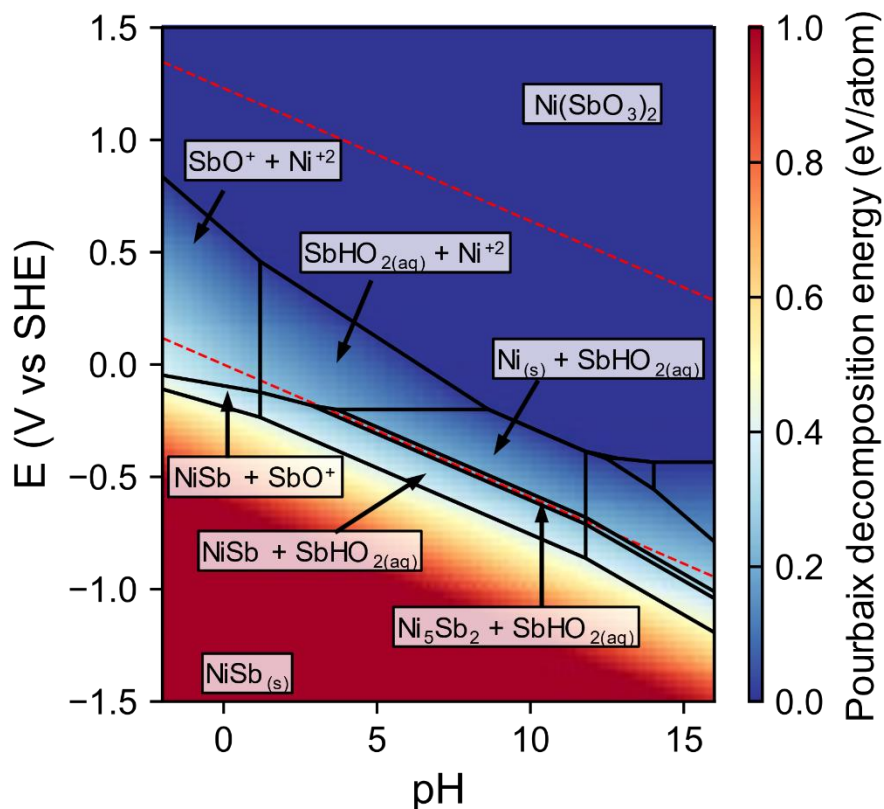


Figure S1: Pourbaix analysis of NiSb_2O_6 . Computationally predicted Pourbaix diagram of Ni-Sb-O using MP data augmented with NiSb_2O_6 rutile phase at a ratio of Ni:Sb = 1:2. The total ion concentration is fixed at 10^{-6} M. The Gibbs free energy of $\text{Ni}(\text{SbO}_3)_2$ decomposition with respect to the Pourbaix stable phases is superimposed on the diagram and represented by the color bar. The thermodynamic stability window of $\text{Ni}(\text{SbO}_3)_2$ extends from approximately 0.5 V vs RHE and above and across all pH. The two red dashed lines denote 0 and 1.23 V vs RHE, respectively.

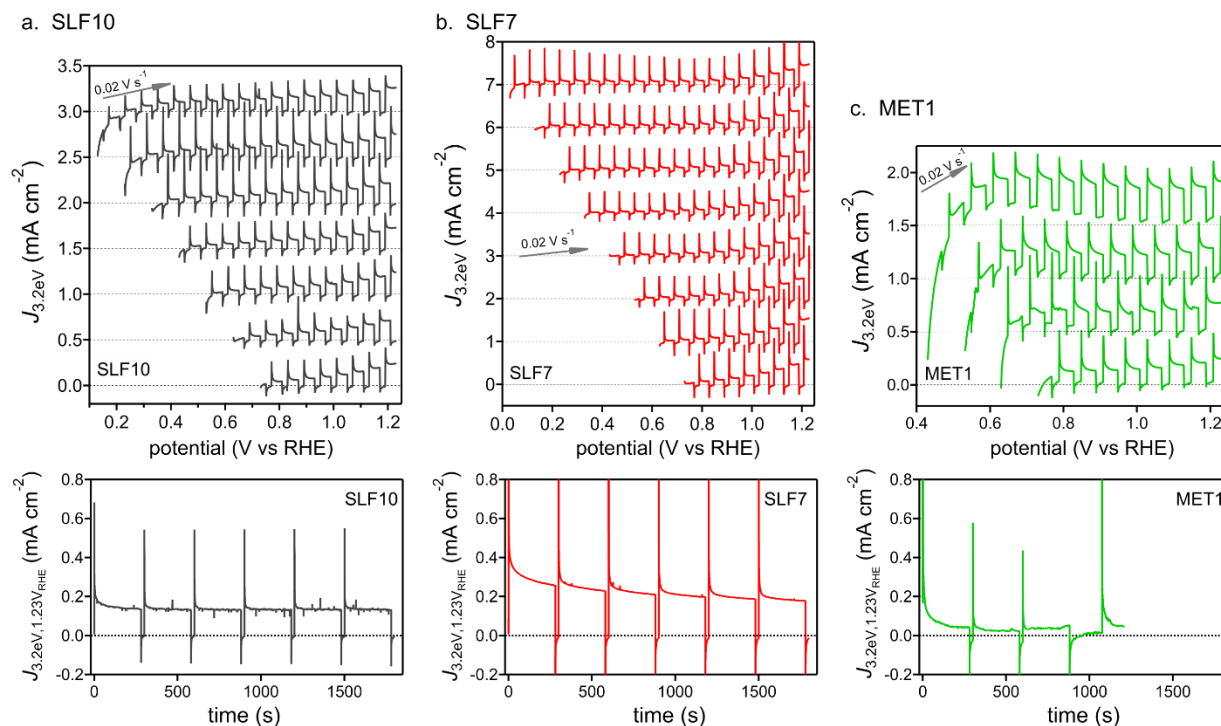


Figure S2. PEC data in pH 1, 3, and 10. A series of anodic chopped-illumination CV sweeps of am-NiSbO_z thin film photoanodes under 3.2 eV illumination in 3 electrolytes: a) SLF10, b) SLF7, and c) MET1, respectively, followed by a CA at the applied potential of 1.23 V vs RHE. The photocurrent degrades on 10² s scale in pH 1, 10³ s scale in pH 7, and >>10³ s scale in pH 10.

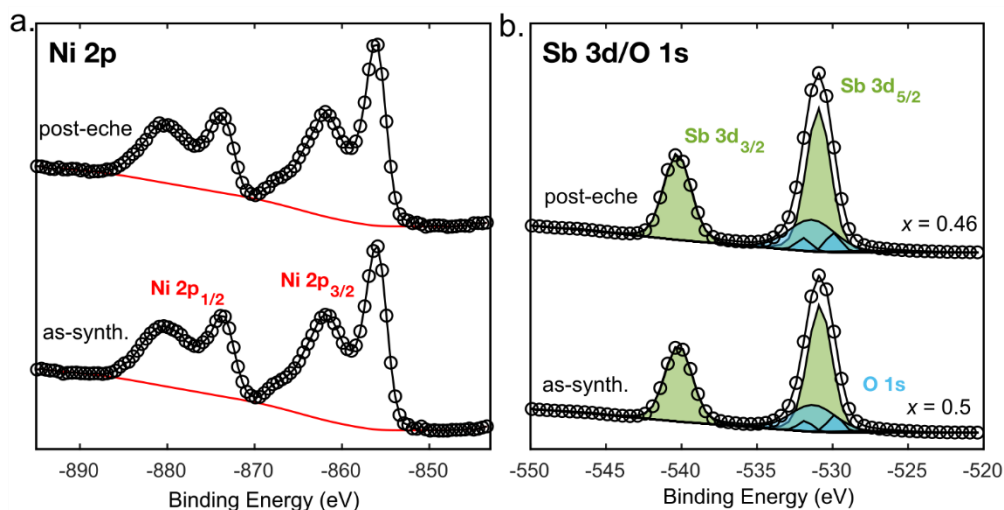


Figure S3. XPS analysis. XPS spectra for the am-NiSbO_z sample before (as-synth.) and after (post-eche) 30 min photoelectrochemical stability measurement (Fig. 4b) in pH 10 at applied potential of 1.23 V vs RHE under 3.2 eV LED illumination. (a) Ni 2p and (b) Sb 3d/O 1s spectra used for the quantification of Ni:Sb near-surface composition. For the as-synthesized thin film, the Ni surface composition was $x = 0.5$ the same to the bulk composition determined from XRF, and was $x = 0.46$ Sb-rich after PEC operation.

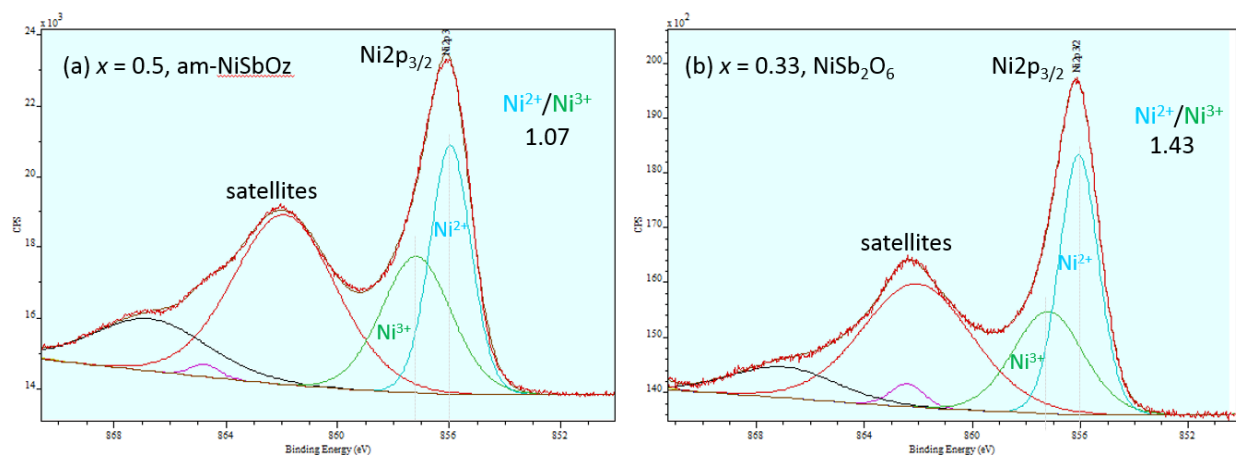


Figure S4. XPS fitting for Ni. The high-resolution core-level Ni $2p_{3/2}$ XPS spectra of Ni $_x$ Sb $_{1-x}$ O $_z$ thin film photoanodes: (a) $x = 0.5$, as-synthesized am-NiSbO $_z$, and (b) $x = 0.33$, as-synthesized NiSb $_2$ O $_6$. Deconvoluted Ni $2p_{3/2}$ XPS using Gaussian-Lorentzian function represents 2 peaks with binding energies of 856.0 and 857.2 eV, which are related to Ni $^{2+}$ (OH) $_2$ and Ni $^{3+}$ OOH, respectively, according to the literature values. [<http://www.xpsfitting.com/2012/01/nickel.html>]. The Ni $^{2+}$ /Ni $^{3+}$ ratio was directly calculated from the area under each spectrum peak.

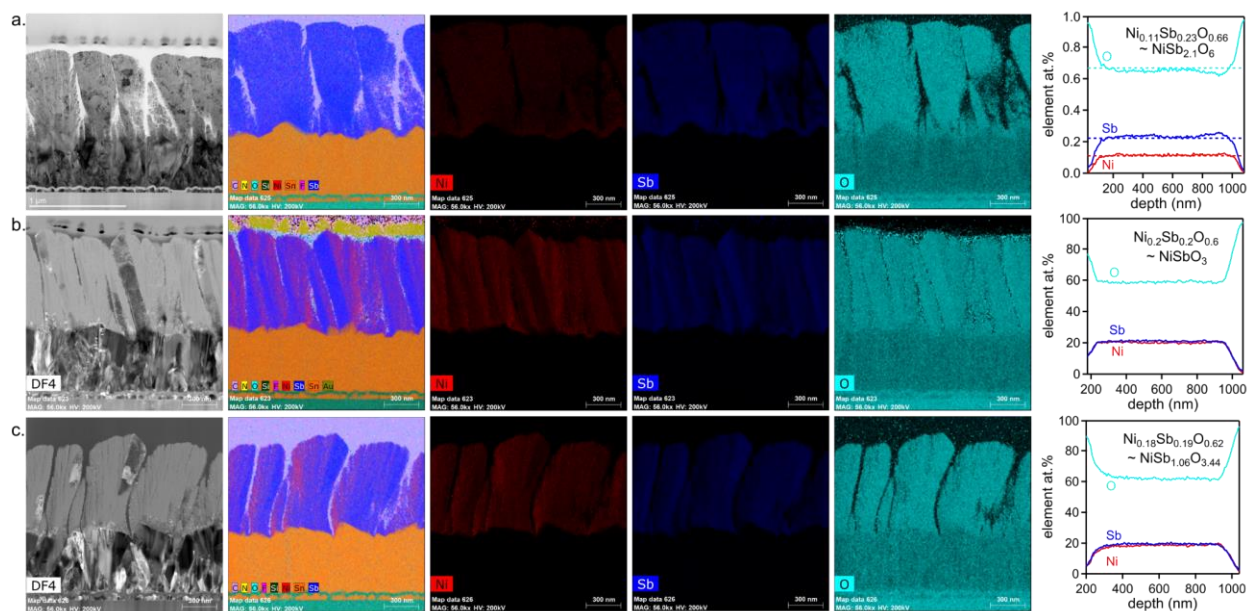


Figure S5: TEM characterization. The bright-field cross-section TEM images and the corresponding energy dispersive x-ray spectroscopy (EDX) elemental mapping and depth profiles of Ni $_x$ Sb $_{1-x}$ O $_z$ thin film photoanodes: (a) $x = 0.33$, as-synthesized NiSb $_2$ O $_6$, (b) $x = 0.5$, as-synthesized am-NiSbO $_z$, and (c) $x = 0.5$, am-NiSbO $_z$ after 30 mins operation under the applied potential of 1.23 V vs RHE in pH 10 electrolyte.

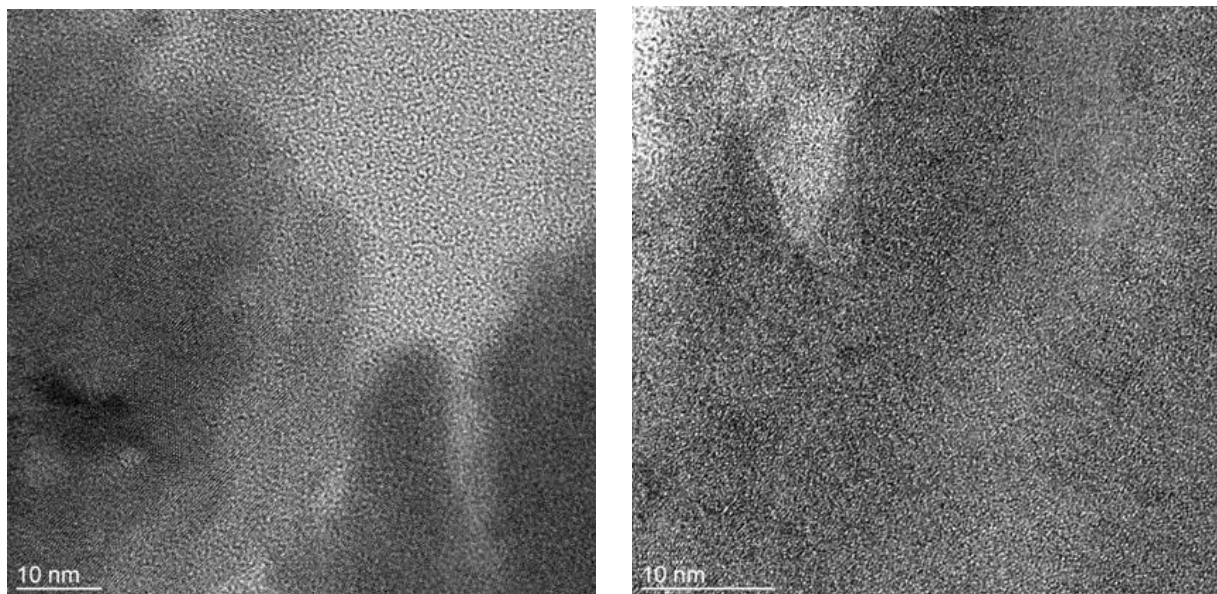


Figure S6: HRTEM images. HRTEM images of $\text{Ni}_x\text{Sb}_{1-x}\text{O}_z$ ($x = 0.5$) thin film after 30 mins operation under the applied potential of 1.23 V vs RHE in pH 10 electrolyte reveal no lattice fringes. This observation combined with XRD and SAED analysis together demonstrates the disordered atomic arrangement and the formation of amorphous Ni-Sb oxide (denoted as am-NiSbO₂). There is no discernible passivation layer.

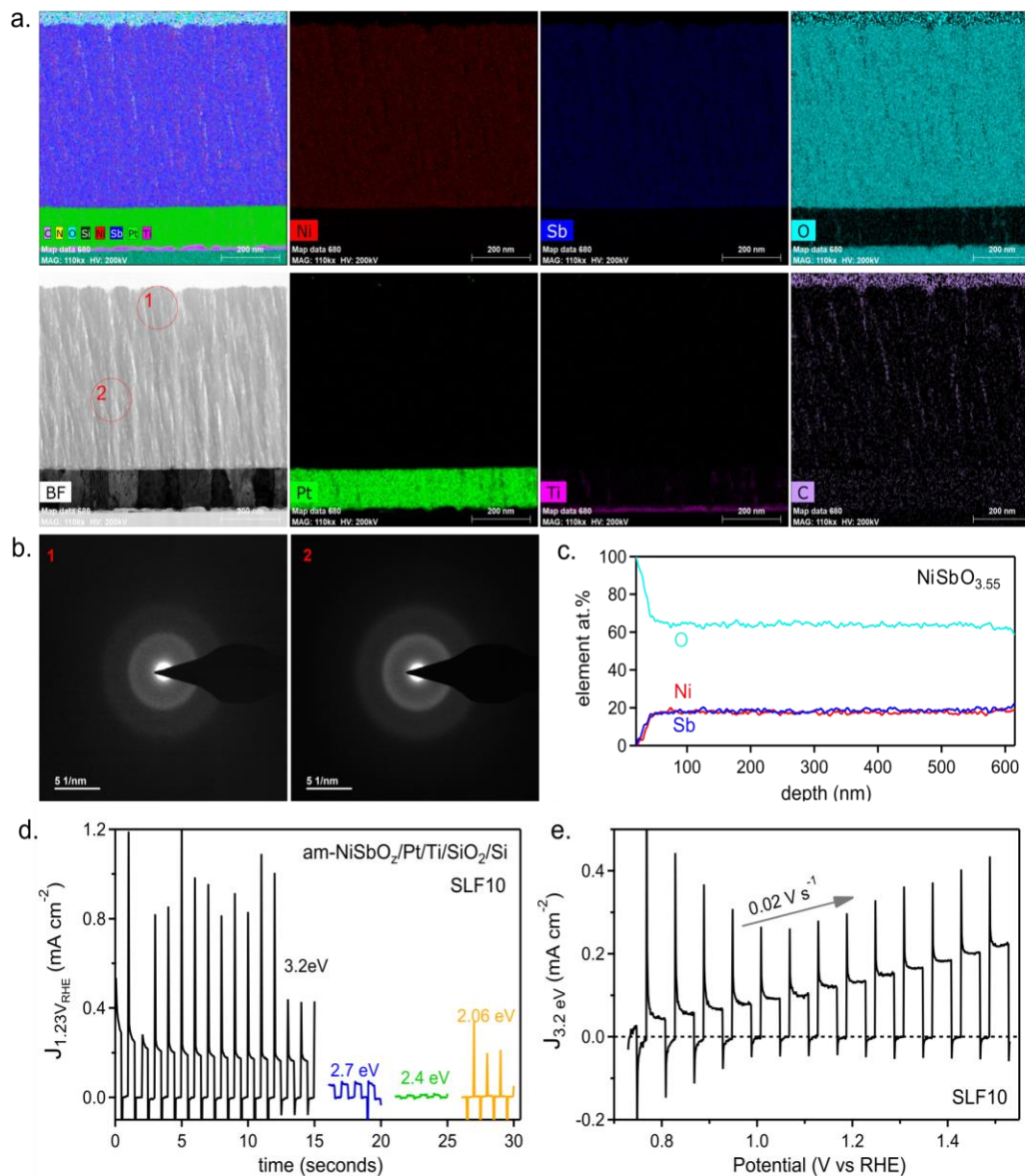


Figure S7. TEM and PEC on lower-surface-area sample. Characterization of am-NiSbO_z thin film photoanode deposited on Pt/Ti/SiO₂/Si substrate and subsequently annealed at 610 °C in air. (a) The bright-field cross-section TEM images and the corresponding energy dispersive x-ray spectroscopy (EDX) elemental mapping; (b) two selected area (indicated by red circle 1 and 2) electron diffraction (SAED) images showing diffuse rings that indicate the presence of amorphous materials; (c) the depth profile of Ni, Sb, and O elemental concentrations cross the film thickness indicating the value of *z* is about 3.55; (d) Chopped-illumination CA measured under 4 illumination sources in the SLF10 electrolyte under the applied potential of 1.23 V vs RHE, followed by a CV sweep under 3.2 eV illumination at a rate of 0.02 V s⁻¹. The anodic sweep is shown in (e). These results demonstrate that the nanostructure and lateral composition inhomogeneities of Figure 5 and S4 arise from deposition on a rough substrate and that photoactivity is not reliant on either of the morphological aspects of the photoanode. Conversely, the photocurrent is approximately 4× lower for this film on Pt compared to Figure 1, likely due to the relatively high surface area of the film deposited on F-doped SnO₂.

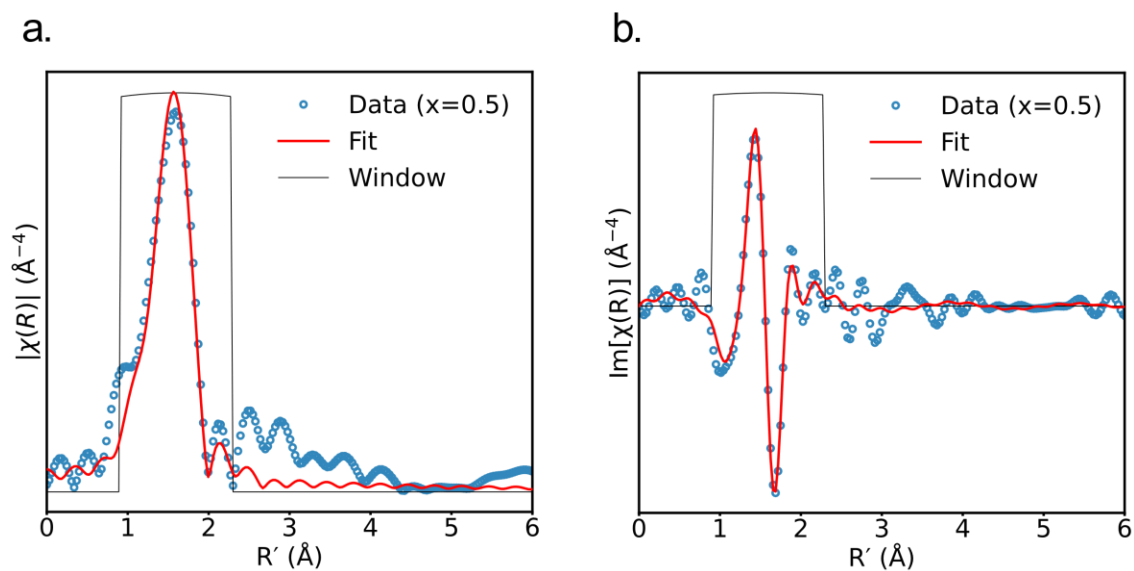


Figure S8. EXAFS analysis for Ni:Sb=1:1. EXAFS single-shell analysis of as-synthesized $\text{Ni}_x\text{Sb}_{1-x}\text{O}_z$ photoanodes at Ni concentration of $x = 0.5$ (am- NiSbO_z) at Ni K-edge. Total fit signal (red line) superimposed on the experimental signal (blue dot).

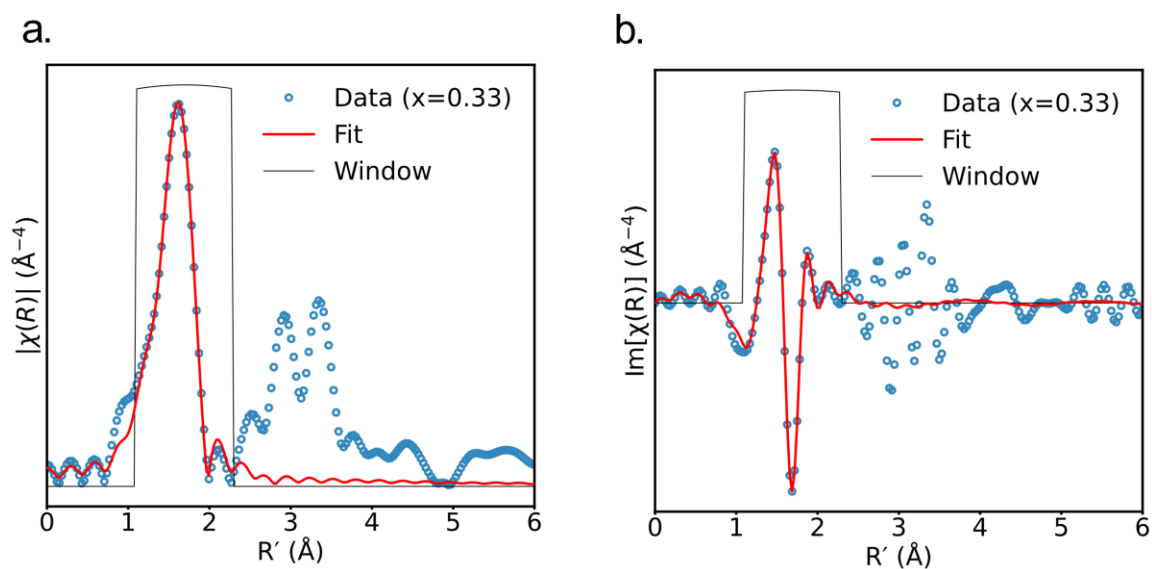


Figure S9. EXAFS analysis for Ni:Sb=1:2. EXAFS single-shell analysis of as-synthesized $\text{Ni}_x\text{Sb}_{1-x}\text{O}_z$ photoanodes at Ni concentration of $x = 0.33$ (NiSb_2O_6) at Ni K-edge. Total fit signal (red line) superimposed on the experimental signal (blue dot).

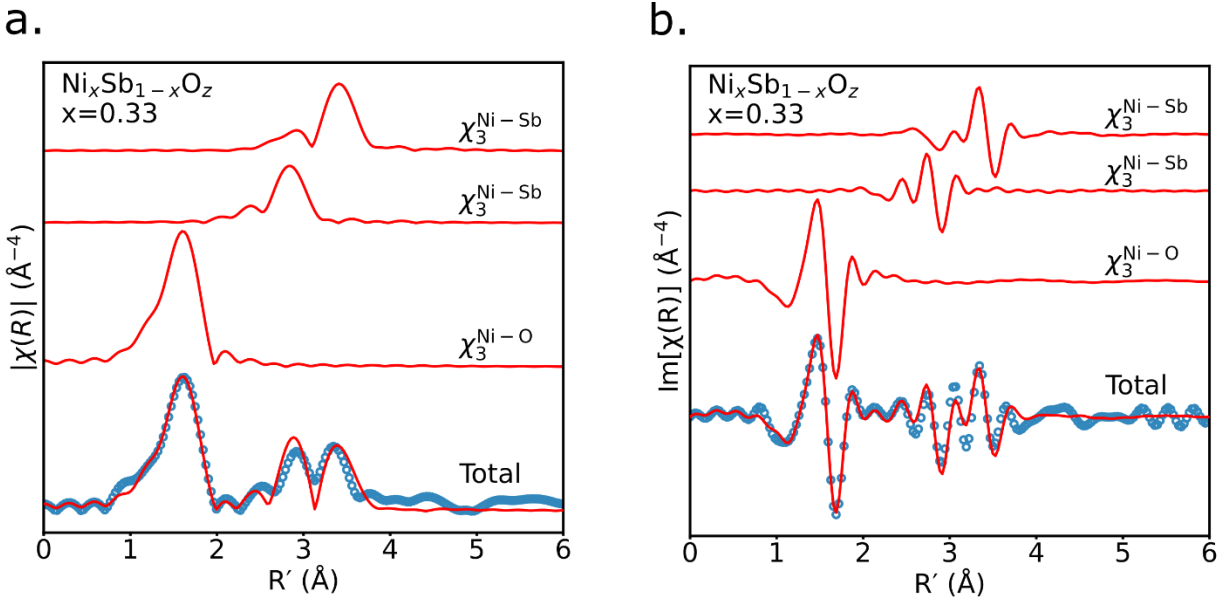


Figure S10. EXAFS multiple-shell analysis. Multiple-shell fitting of the a) real and b) imaginary components on the Ni K-edge EXAFS signal for as-synthesized $\text{Ni}_x\text{Sb}_{1-x}\text{O}_z$ photoanodes at Ni concentration of $x = 0.33$ (NiSb_2O_6). Curves from top to bottom are backscattering signals χ_3 of different paths, and total fit signal (red line) superimposed on the experimental signal (blue dot).

Table S4. EXAFS fitting results. EXAFS fits of as-synthesized $\text{Ni}_x\text{Sb}_{1-x}\text{O}_z$ photoanodes at Ni concentration of $x = 0.33$ (NiSb_2O_6) and 0.5 (am- NiSbO_2). Fit #1: Single-shell fit of $x = 0.5$ (am- NiSbO_2); Fit #2: single-shell fit of $x = 0.33$ (NiSb_2O_6); Fit #3: multiple-shell fit of $x = 0.33$ (NiSb_2O_6).

Fit #	Sample	Path	R (Å)	CN	$\sigma^2 \times 10^3$ (Å ²)	ΔE_0 (eV)	R factor
1	$\text{Ni}_x\text{Sb}_{1-x}\text{O}_z$ ($x = 0.5$)	Ni-O	2.02 ± 0.01	5.02 ± 0.72	8 ± 1	-0.03 ± 1.55	0.012
2	$\text{Ni}_x\text{Sb}_{1-x}\text{O}_z$ ($x = 0.33$)	Ni-O	2.04 ± 0.01	5.53 ± 0.30	6 ± 1	0.55 ± 0.65	0.005
3	$\text{Ni}_x\text{Sb}_{1-x}\text{O}_z$ ($x = 0.33$)	Ni-O	2.03 ± 0.01	5.73 ± 1.27	6 ± 2	-0.28 ± 1.64	0.07
		Ni-Sb	3.06 ± 0.02	2	8 ± 2		
		Ni-Sb	3.66 ± 0.02	8	12 ± 2		

For the multiple-shell fitting of $\text{Ni}_x\text{Sb}_{1-x}\text{O}_z$ ($x = 0.33$) sample, FEFF paths were generated using a NiSb_2O_6 crystal structure with mp-505271. Due to the complexity of the 2+ shell on the NiSb_2O_6 model (multiple single-scattering and multiple-scattering paths), besides the first-shell Ni-O path, we chose the two major Ni-Sb paths during the fit and fixed the Ni-Sb coordination numbers (2 and 8, respectively) to match with the computational NiSb_2O_6 structure (mp-505271) and fit the coordination distance and test whether the NiSb_2O_6 model would match. The first shell Ni-O coordination number is fitted as 5.02 ± 0.72 , and distance is 2.03 ± 0.01 Å, which is comparable to the Ni-O coordination number of 6 and distance of 2.07 Å for the computational NiSb_2O_6 structure (mp-505271). The coordination distance of two Ni-Sb paths are fitted as 3.06 and 3.66 Å, respectively, which is comparable to the 3.11 and 3.69 Å of the NiSb_2O_6

structure (mp-505271). The overall well-matched fitting shows that the $\text{Ni}_x\text{Sb}_{1-x}\text{O}_z$ ($x = 0.33$) is well aligned with the NiSb_2O_6 model (mp-505271).

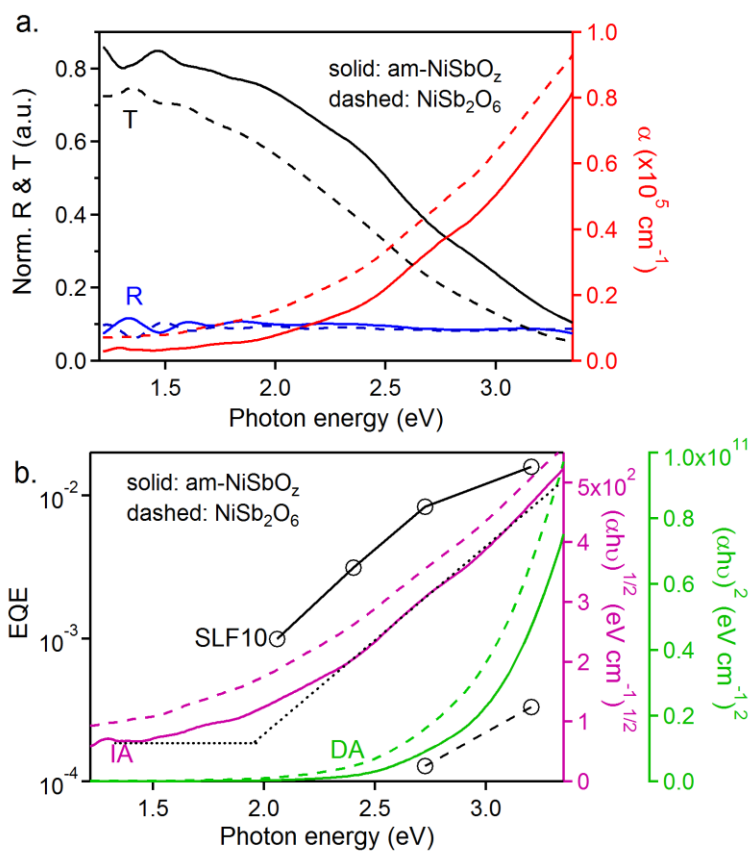


Figure S11. Optical characterization of am-NiSbO_z and NiSb₂O₆. (a) The normalized transmittance T, normalized total reflectance R, and absorption coefficient α are shown where for each spectrum the solid and dashed lines correspond to am-NiSbO_z and NiSb₂O₆, respectively. (b) Spectral EQE at the applied potential of 1.23 V vs RHE in SLF10 electrolyte and Tauc signals, where the EQE (left) and the direct allowed (DA) and indirect allowed (IA) Tauc signals each have a dedicated vertical axis. To best approximate the intrinsic spectral absorption, these calculations were performed using thicknesses of 270 and 310 nm for am-NiSbO_z and NiSb₂O₆, respectively, which were calculated from the XRF measurement of molar content of Ni and Sb using weighted molar densities of NiO and Sb₂O₅. This model for thickness corresponds to the thickness of a perfectly dense film. The TEM images of Figure 5 indicate the thickness of the film, which contains a substantial void density, is up to 2 \times larger. Using this thickness would lead to a down-scaling of the absorption coefficient and Tauc signals but would not alter the conclusions drawn from this optical spectroscopy data.

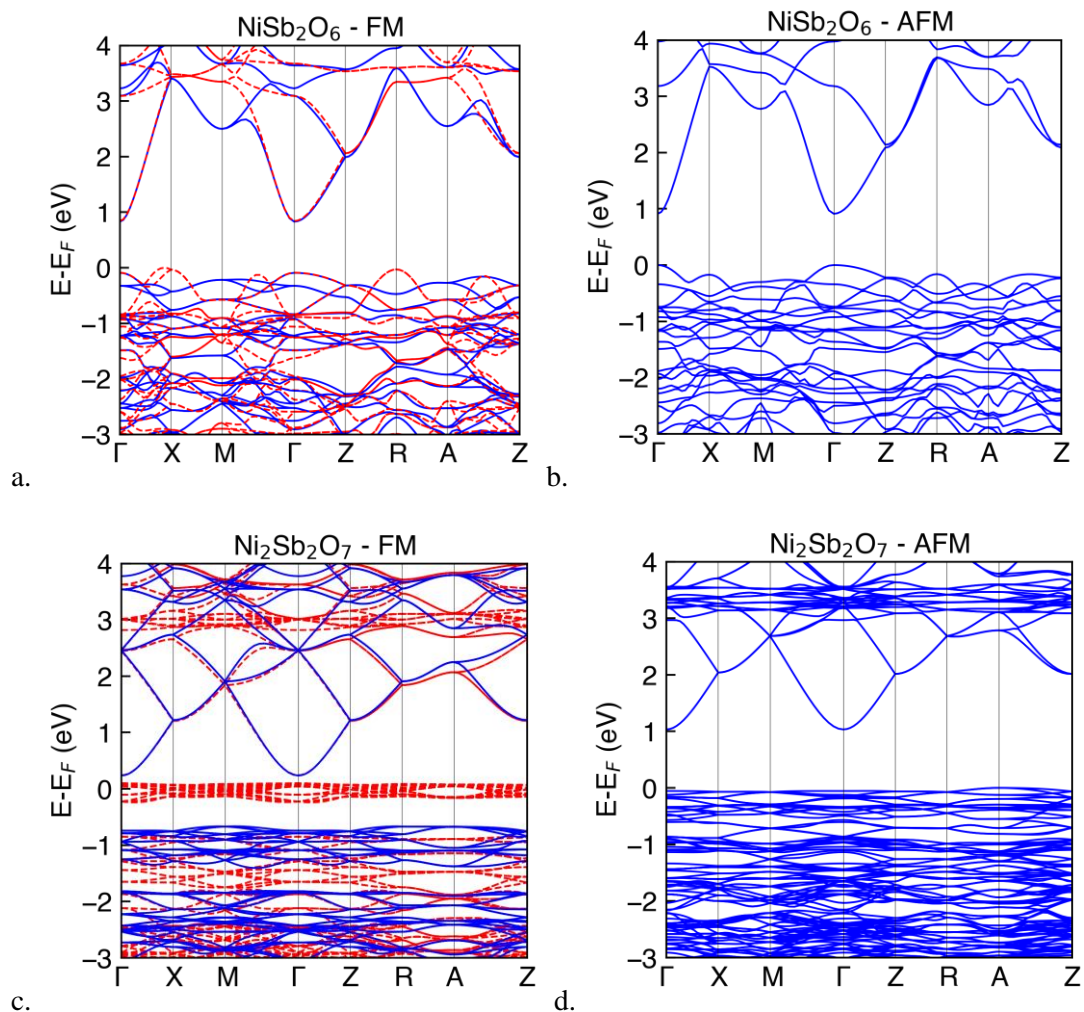


Figure S12. DFT band structures for NiSb₂O₆. Band structures are shown for (a) FM ordering of Ni ions and (b) AFM ordering of Ni spins and for Ni₂Sb₂O₇ with (c) FM ordering and (d) the lowest energy AFM ordering. All cases except for the FM ordering of NiSb₂O₆ (which is metallic) are characterized by highly dispersive conduction bands. Both AFM band structures are characterized by direct gaps at the Gamma point and the FM band structure of Ni₂Sb₂O₇ has a slightly indirect band gap from R to Gamma. For the FM ordered band structures, red dotted lines and solid blue lines represent the up and down spin channels.

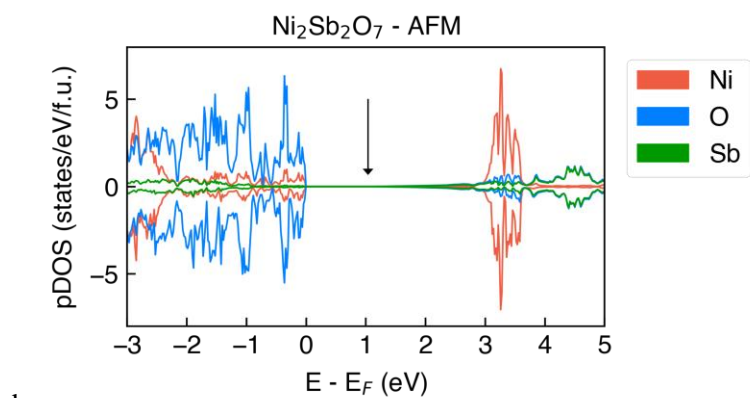
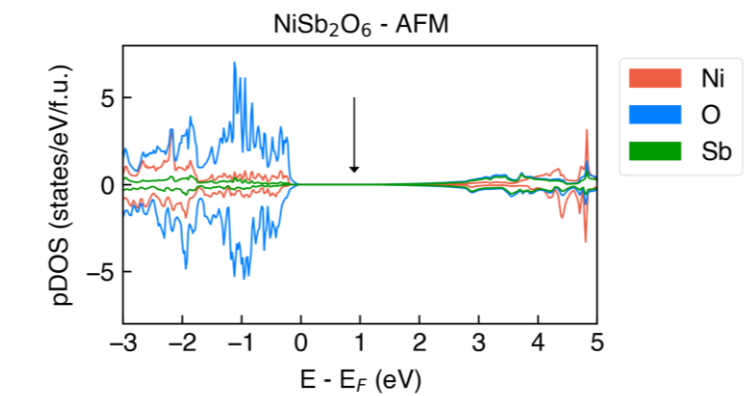


Figure S13. Comparison of pDOS. DFT projected density of states per formula unit for (a) NiSb₂O₆ and (b) Ni₂Sb₂O₇ in the AFM magnetic ordering. Arrows indicate the onset of a nonzero density of states in the conduction band.

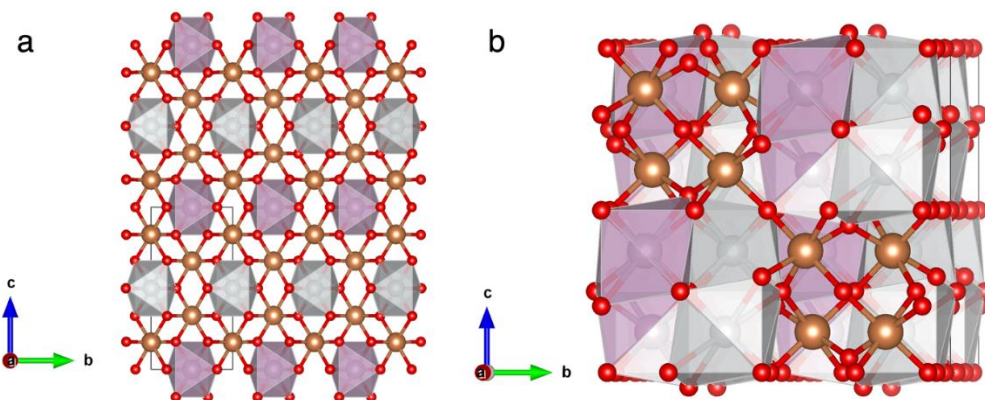


Figure S14. Crystal structures for DFT calculations. Crystal structures of (a) NiSb_2O_6 and (b) $\text{Ni}_2\text{Sb}_2\text{O}_7$ in their lowest energy AFM configurations. Ni ions are in purple and grey, with the two colors indicating up and down magnetic moments. Sb ions are in gold and O atoms are in red. For each material, two AFM magnetic orderings were selected. For NiSb_2O_6 the Ni octahedra are not connected. Planes of disconnected Ni octahedra in the ab-plane are layered with each plane offset by half a lattice parameter, making triangles with an in-plane separation of $\sim 4.7 \text{ \AA}$ and out-of-plane separations $\sim 5.7 \text{ \AA}$ apart. The two AFM orderings investigated were (1) FM ordering in-plane and AFM ordering between neighboring planes (Fig. S14a) and (2) FM ordering along diagonals with AFM ordering between neighboring in-plane Ni octahedra. The most stable AFM ordering was the first, with FM ordering in-plane and AFM ordering between neighboring planes. For $\text{Ni}_2\text{Sb}_2\text{O}_7$ the magnetic ordering is substantially more complex, as prior experimental evidence indicates that this material is a frustrated antiferromagnet⁵³. Investigation of various noncollinear magnetic orderings would be more appropriate for identifying the ground state magnetic ordering of $\text{Ni}_2\text{Sb}_2\text{O}_7$ but that is beyond the scope of this work. Ni sites are clustered in groups of four with edge-sharing polyhedra. The AFM orderings considered were (1) FM ordering within each cluster of four edge-sharing polyhedra and AFM ordering between clusters and (2) two of the polyhedra in each cluster with parallel magnetic moments and the other two with their magnetic moments in the opposite direction (Fig S14b). The second ordering was more energetically stable. Relative energies of the most stable AFM orderings and the FM ordering are displayed in Table S5.

Table S5. DFT and structure parameters. DFT-PBE+U energies, band gaps, and lattice parameters of NiSb₂O₆ and Ni₂Sb₂O₇. The energies of both materials exhibit a strong dependence on magnetic ordering. The energetic stability of these materials is very sensitive to magnetic ordering. The AFM ordering is 71 meV/atom and 213 meV/cation lower in energy than the FM ordering for NiSb₂O₆. The AFM ordering is 231 meV/atom and 636 meV/cation lower in energy than the FM ordering for Ni₂Sb₂O₇.

	mp-id	Magnetic ordering	Energy (eV/atom)	Energy (eV/cation)	PBE+U Band Gap (eV)	a,b (Å)	c (Å)
NiSb ₂ O ₆	mp-505271	FM	-5.846	-17.537	0.829	4.716	9.360
		AFM	-5.917	-17.750	0.912	4.717	9.363
Ni ₂ Sb ₂ O ₇	mp-1190650	FM	-5.313	-14.610	0	10.145	10.145
		AFM	-5.544	-15.246	1.0335	10.182	10.112

Table S6. Literature context. Comparison of dissolved metals concentrations in electrolyte after photoelectrochemical treatment at the applied potential of 1.23 V vs RHE over the course of 20 to 240 mins. This work used a Doric 385 nm LED (7.2 mW cm⁻²), while others used AM 1.5 1 sun illumination (100 mW cm⁻²).

Photoanode	Duration (min)	pH	electrolyte	Dissolved metal concentrations (μmol L ⁻¹)			Literature this work	
				Ni	Sb	Tot.		
am-NiSbO _z	30	10	0.1 M boric buffer	0.02	0.001	0.021		
α-SnWO ₄				Sn	W	Tot.	Schnell2022 ¹	
	60	2	0.1 M HCl/KCl	0.94	0.13	1.07		
	60	7	0.5 M KPi	0.86	0.29	1.15		
	60	9	0.5 M KPi	10	7	17		
	60	13	0.1 M KOH	22	22	44		
WO ₃				W		Tot.	Le2021 ²	
	30	0.3	0.5 M H ₂ SO ₄	0.87		0.87		
	30	5.8	0.1 M Na ₂ SO ₄	2.3		2.3		
	30	5.8	0.1 M KPi	9.57		9.57		
	30	7	0.1 M KPi	89.04		89.04		
BiVO ₄				Bi	V	Tot.	Toma2016 ³	
	60	6.8	0.1 M KPi	0	0.08	0.08		
	60	6.8	1 M KPi	0.55	0.57	1.12		
	20	12.3	0.1 M KPi	0.1	0.29	0.39		
	20	12.3	1 M KPi	1.57	1.48	3.05		
	20	13	0.1 M NaOH	0.17	0.32	0.49		
	20	14	1 M NaOH	0.71	2.2	2.91		
Mo : BiVO ₄				Bi	V	Mo	Tot.	Yao2019 ⁴
	240	5.7	0.1 M Na ₂ SO ₄	0.13	2.9	0.09	3.12	
	240	7	0.1 M Na ₂ SO ₄	0.01	1.14	0.07	1.22	
	240	8.3	0.1 M KPi	0.36	14.11	0.2	14.67	

References:

- (1) Schnell, P.; Dela Cruz, J. M. C. M.; Kölbach, M.; van de Krol, R.; Abdi, F. F. PH-Dependent Stability of α -SnWO₄ Photoelectrodes. *Chem. Mater.* **2022**. <https://doi.org/10.1021/acs.chemmater.1c03517>.
- (2) Le, H. V.; Pham, P. T.; Le, L. T.; Nguyen, A. D.; Tran, N. Q.; Tran, P. D. Fabrication of Tungsten Oxide Photoanode by Doctor Blade Technique and Investigation on Its Photocatalytic Operation Mechanism. *International Journal of Hydrogen Energy* **2021**, *46* (44), 22852–22863. <https://doi.org/10.1016/j.ijhydene.2021.04.113>.
- (3) Toma, F. M.; Cooper, J. K.; Kunzelmann, V.; McDowell, M. T.; Yu, J.; Larson, D. M.; Borys, N. J.; Abelyan, C.; Beeman, J. W.; Yu, K. M.; Yang, J.; Chen, L.; Shaner, M. R.; Spurgeon, J.; Houle, F. A.; Persson, K. A.; Sharp, I. D. Mechanistic Insights into Chemical and Photochemical Transformations of Bismuth Vanadate Photoanodes. *Nat Commun* **2016**, *7* (1), 12012. <https://doi.org/10.1038/ncomms12012>.
- (4) Yao, X.; Zhao, X.; Hu, J.; Xie, H.; Wang, D.; Cao, X.; Zhang, Z.; Huang, Y.; Chen, Z.; Sritharan, T. The Self-Passivation Mechanism in Degradation of BiVO₄ Photoanode. *iScience* **2019**, *19*, 976–985. <https://doi.org/10.1016/j.isci.2019.08.037>.